Power System Protection and Control
ISSN:1674-3415

AI-BASED RADIOGENOMIC MODELS FOR PREDICTING IMMUNOTHERAPY RESPONSE IN SOLID TUMORS

Dr. Ohmini Krishnamurthy Rajendran

MBBS, Post graduate (MD Radiodiagnosis), KIMS Hospital and Research Centre, Krishna Rajendra Road , Parvathipuram, Vishweshwarapura, Basavanagudi, Bengaluru, Karnataka 560004
jsmnk4@gmail.com

Recevied: 20 September 2023 **Revised**:30 October 2023 **Accepted**: 24 November 2023

ABSTRACT

The integration of artificial intelligence with radiogenomics represents a transformative approach in precision oncology, particularly for predicting immunotherapy response in solid tumors. This study develops and validates deep learning-based radiogenomic models that combine medical imaging features with genomic biomarkers to predict patient responses to immune checkpoint inhibitors. We analyzed data from 342 patients with non-small cell lung cancer, melanoma, and renal cell carcinoma who received anti-PD-1/PD-L1 therapy between 2018 and 2022. Our convolutional neural network architecture integrated CT imaging radiomics with tumor mutational burden, PD-L1 expression, and gene expression profiles. The proposed model achieved an area under the curve of 0.87 for predicting complete or partial response, significantly outperforming clinical models (AUC = 0.64, $p < 0.001$). Feature importance analysis revealed that radiomic texture features combined with TMB scores contributed most substantially to prediction accuracy. This research demonstrates that AI-driven radiogenomic models can provide non-invasive, cost-effective tools for patient stratification in immunotherapy, potentially reducing treatment-related toxicities and healthcare costs while improving clinical outcomes.

***Keyword**: Radiogenomics, Artificial Intelligence, Immunotherapy, Deep Learning, Precision Oncology, Biomarker Prediction, Solid Tumors*

INTRODUCTION

Cancer immunotherapy has revolutionized oncological treatment paradigms over the past decade, offering durable responses and improved survival rates for patients with previously intractable solid tumors (Sharma et al., 2017). Immune checkpoint inhibitors targeting PD-1, PD-L1, and CTLA-4 pathways have demonstrated remarkable efficacy across multiple cancer types, including melanoma, non-small cell lung cancer, and renal cell carcinoma (Ribas et al., 2016). However, clinical implementation faces a critical challenge: only 20-40% of patients respond to these therapies, while others experience disease progression, immune-related adverse events, and substantial financial burden without therapeutic benefit (Topalian et al., 2019).

Current predictive biomarkers, including PD-L1 expression and tumor mutational burden, demonstrate limited accuracy and require invasive tissue biopsies (Davis et al., 2019). These limitations have catalyzed research into alternative approaches that leverage medical imaging and molecular profiling. Radiogenomics, an emerging field that correlates imaging phenotypes with genomic characteristics, offers a non-invasive method to characterize tumor biology (Gillies et al., 2016). The integration of artificial intelligence, particularly deep learning architectures, enables extraction of quantitative imaging features beyond human perception and identification of complex patterns across multimodal datasets (Esteva et al., 2019).

Despite promising preliminary studies, several knowledge gaps persist. First, most radiogenomic research focuses on diagnosis or prognosis rather than treatment response prediction. Second, existing models typically analyze imaging or

DOI: 10.46121/pspc.51.4.4

genomic data independently, failing to capture synergistic information. Third, interpretability remains limited, hindering clinical translation and physician trust (Zaharchuk et al., 2018). This research addresses these gaps by developing an integrated AI-based radiogenomic framework that combines CT imaging features with genomic biomarkers to predict immunotherapy response in solid tumors.

The primary research question guiding this investigation is: Can multimodal deep learning models integrating radiomics and genomics predict immunotherapy response more accurately than conventional biomarkers? Secondary questions examine which imaging and molecular features contribute most significantly to prediction accuracy and whether model performance varies across different tumor types.

LITERATURE REVIEW

The landscape of predictive biomarkers in cancer immunotherapy has evolved substantially since the initial approval of checkpoint inhibitors. Early studies established PD-L1 expression as a predictive marker, though subsequent research revealed significant limitations (Borghaei et al., 2015). PD-L1 immunohistochemistry demonstrates high intratumoral heterogeneity, variable assay platforms, and inconsistent threshold definitions, resulting in prediction accuracies rarely exceeding 65% (Patel et al., 2018).

Tumor mutational burden emerged as an alternative biomarker based on the hypothesis that tumors with higher neoantigen loads elicit stronger immune responses (Rizvi et al., 2015). The FDA's tissue-agnostic approval of pembrolizumab for TMB-high tumors validated this approach, yet TMB alone demonstrates area under curve values of 0.60-0.70 across most tumor types (Goodman et al., 2017). These modest performance metrics underscore the need for more comprehensive predictive frameworks.

Radiomics, defined as high-throughput extraction of quantitative features from medical images, has demonstrated capacity to capture tumor phenotypic characteristics invisible to radiologist interpretation (Lambin et al., 2017). First-order statistics describe intensity distributions, while texture features quantify spatial patterns. Studies have correlated radiomic signatures with genetic mutations, including EGFR and KRAS alterations in lung adenocarcinoma (Aerts et al., 2014). However, most radiomic research in immunotherapy context remains exploratory, with limited validation cohorts. The convergence of artificial intelligence and medical imaging has accelerated dramatically. Convolutional neural networks excel at automated feature extraction from images, eliminating manual feature engineering (LeCun et al., 2015). Transfer learning approaches utilizing models pre-trained on ImageNet have proven effective for medical imaging tasks despite limited training data (Shin et al., 2016). Attention mechanisms enable models to highlight relevant image regions, enhancing interpretability (Selvaraju et al., 2017).

Integration of multimodal data represents the next frontier in precision oncology. Sun et al. (2018) demonstrated that combining clinical, imaging, and genomic features improved survival prediction in glioblastoma patients. Trebeschi et al. (2019) developed radiomics models predicting microsatellite instability status, a biomarker relevant to immunotherapy response, achieving AUC of 0.74 in colorectal cancer. Yet comprehensive frameworks integrating radiomics, genomics, and deep learning for immunotherapy prediction remain sparse.

The theoretical foundation for radiogenomic correlation rests on the premise that genetic alterations drive phenotypic changes visible in medical imaging. Tumor metabolism, vascularity, and architectural organization reflect underlying molecular processes (Rutman et al., 2013). Machine learning algorithms can detect these subtle associations across high-dimensional feature spaces that exceed human analytical capacity.

Current gaps include limited prospective validation, unclear generalizability across institutions with varying imaging protocols, and insufficient exploration of temporal dynamics as tumors evolve during treatment. Additionally, most studies focus on single cancer types, leaving questions about pan-cancer applicability unanswered. This research advances the field by developing interpretable, validated models applicable across multiple solid tumor types.

DOI: 10.46121/pspc.51.4.4

METHODOLOGY

Study Design and Patient Cohort

This retrospective cohort study analyzed data from 342 patients diagnosed with stage III-IV solid tumors who received anti-PD-1 or anti-PD-L1 immunotherapy at three tertiary cancer centers between January 2018 and December 2022. The cohort comprised 156 non-small cell lung cancer patients, 112 melanoma patients, and 74 renal cell carcinoma patients. Inclusion criteria required baseline CT imaging within 4 weeks before treatment initiation, available tissue specimens for genomic analysis, and minimum 6-month follow-up. Exclusion criteria included prior immunotherapy exposure, concurrent systemic therapy, and inadequate image quality. Response assessment followed RECIST 1.1 criteria at 3-month intervals.

Data Collection and Processing

Imaging Data: Contrast-enhanced CT scans were acquired using institutional protocols with slice thickness 1-3mm. Images underwent preprocessing including intensity normalization, resampling to 1mm³ isotropic voxels, and tumor segmentation. Two radiologists independently delineated tumor volumes using 3D Slicer software, with discrepancies resolved through consensus review.

Genomic Data: Next-generation sequencing was performed on formalin-fixed paraffin-embedded specimens using comprehensive genomic profiling panels covering 324-468 genes. Tumor mutational burden was calculated as mutations per megabase. PD-L1 expression was assessed via immunohistochemistry using validated assays (22C3, 28-8, or SP263 antibodies). RNA sequencing data provided gene expression profiles for immune-related pathways.

Clinical Data: Electronic medical records provided demographic information, performance status, prior treatments, and outcome data. Overall survival and progression-free survival were calculated from treatment initiation.

Feature Extraction

Radiomic features were extracted using PyRadiomics library following Image Biomarker Standardization Initiative guidelines. We computed 107 features across categories:

- **First-order statistics (19 features):** Mean intensity, variance, skewness, kurtosis, energy
- **Shape features (14 features):** Volume, surface area, sphericity, compactness
- **Texture features (74 features):** Gray Level Co-occurrence Matrix (GLCM), Gray Level Run Length Matrix (GLRLM), Gray Level Size Zone Matrix (GLSZM), Gray Level Dependence Matrix (GLDM)

The mathematical formulation for representative features:

GLCM Contrast: $\text{Contrast} = \sum_{i=1}^{N_g} \sum_{j=1}^{N_g} (i-j)^2 p(i,j)$

GLRLM Run Length Non-Uniformity: $\text{RLN} = \frac{\sum_{j=1}^{N_r} \left(\sum_{i=1}^{N_g} p(i,j) \right)^2}{N_r}$

where N_g represents gray levels, N_r represents run lengths, and $p(i,j)$ denotes probability.

Genomic features included TMB (continuous), PD-L1 tumor proportion score (0-100%), expression levels of 50 immune-related genes, and presence of actionable mutations.

Model Architecture

We developed a multimodal deep learning architecture integrating imaging and genomic branches (Figure 1). The imaging branch employed a 3D ResNet-50 backbone pre-trained on video datasets, adapted for volumetric CT data. The genomic branch utilized a fully connected network processing concatenated genomic features. Feature fusion occurred through a cross-attention mechanism enabling dynamic weighting of modality contributions. The final classification layer employed sigmoid activation for binary response prediction.

DOI: 10.46121/pspc.51.4.4

Model equations:

$$h_{img} = \text{ResNet3D}(X_{CT})$$
$$h_{gen} = \text{FC}(X_{genomic})$$
$$\alpha = \text{Softmax}(W_a[h_{img}; h_{gen}])$$
$$h_{fused} = \alpha_1 h_{img} + \alpha_2 h_{gen}$$
$$P(response) = \sigma(W_o h_{fused} + b)$$

where σ represents sigmoid function, W denotes weight matrices, and $[\cdot;\cdot]$ indicates concatenation.

Training and Validation

The dataset was randomly split into training (60%, n=205), validation (20%, n=68), and test sets (20%, n=69), stratified by tumor type and response status. We employed 5-fold cross-validation on the training set for hyperparameter optimization. The model was trained using Adam optimizer with learning rate 0.0001, batch size 16, and binary cross-entropy loss function:

$$\mathcal{L} = -\frac{1}{N}\sum_{i=1}^{N}[y_i \log(\hat{y}_i) + (1 - y_i)\log(1 - \hat{y}_i)]$$

Data augmentation included random rotations (±15°), translations (±10mm), and intensity variations (±10%). Early stopping with patience of 20 epochs prevented overfitting. Training utilized NVIDIA V100 GPUs for approximately 48 hours.

Statistical Analysis

Model performance was evaluated using area under receiver operating characteristic curve, sensitivity, specificity, positive predictive value, and negative predictive value. We compared the proposed model against baseline models using imaging-only, genomics-only, and clinical features through DeLong's test. Feature importance was assessed via SHAP values. Survival analysis employed Kaplan-Meier curves and Cox proportional hazards regression. Statistical significance threshold was set at $p < 0.05$.

Table 1: Patient Characteristics and Clinical Variables

Characteristic	NSCLC (n=156)	Melanoma (n=112)	RCC (n=74)	Total (n=342)
Age (mean ± SD)	64.3 ± 9.1	58.7 ± 12.4	61.2 ± 10.8	61.8 ± 10.9
Male (%)	92 (59%)	68 (61%)	52 (70%)	212 (62%)
ECOG PS 0-1 (%)	124 (79%)	98 (88%)	61 (82%)	283 (83%)
Stage III/IV (%)	48/108 (31/69)	22/90 (20/80)	18/56 (24/76)	88/254 (26/74)
Prior therapy lines (median)	1.2	0.8	1.1	1.0
TMB (mut/Mb, median)	8.4	12.6	5.2	8.7
PD-L1 ≥50% (%)	54 (35%)	38 (34%)	22 (30%)	114 (33%)
Complete/Partial Response (%)	48 (31%)	42 (38%)	26 (35%)	116 (34%)

EXPERIMENTAL SETUP

Hardware and Software Infrastructure

All experiments were conducted on a high-performance computing cluster equipped with dual Intel Xeon Gold 6248R processors (3.0 GHz, 24 cores), 384GB RAM, and four NVIDIA Tesla V100 GPUs (32GB memory each). The deep learning framework utilized PyTorch 1.10.0 with CUDA 11.3 for GPU acceleration. Image processing employed SimpleITK 2.1.0 and PyRadiomics 3.0.1. Statistical analyses were performed using R version 4.1.2 and Python 3.8.

DOI: 10.46121/pspc.51.4.4

Preprocessing Pipeline

The preprocessing workflow consisted of sequential steps ensuring data quality and consistency (Figure 2):

1. **DICOM Import and Conversion:** Raw imaging data was imported and converted to NIfTI format while preserving metadata
2. **Quality Control:** Automated checks identified artifacts, incomplete series, or protocol violations
3. **Registration:** Multi-timepoint scans were rigidly registered to baseline using mutual information metric
4. **Intensity Normalization:** Hounsfield unit values were clipped to [-1000, 400] and normalized to [0,1] range
5. **Tumor Segmentation:** Semi-automated segmentation combined region growing with manual refinement
6. **Feature Extraction:** Radiomic features were computed with batch effect correction applied
7. **Genomic Integration:** Molecular data underwent log2 transformation and standardization

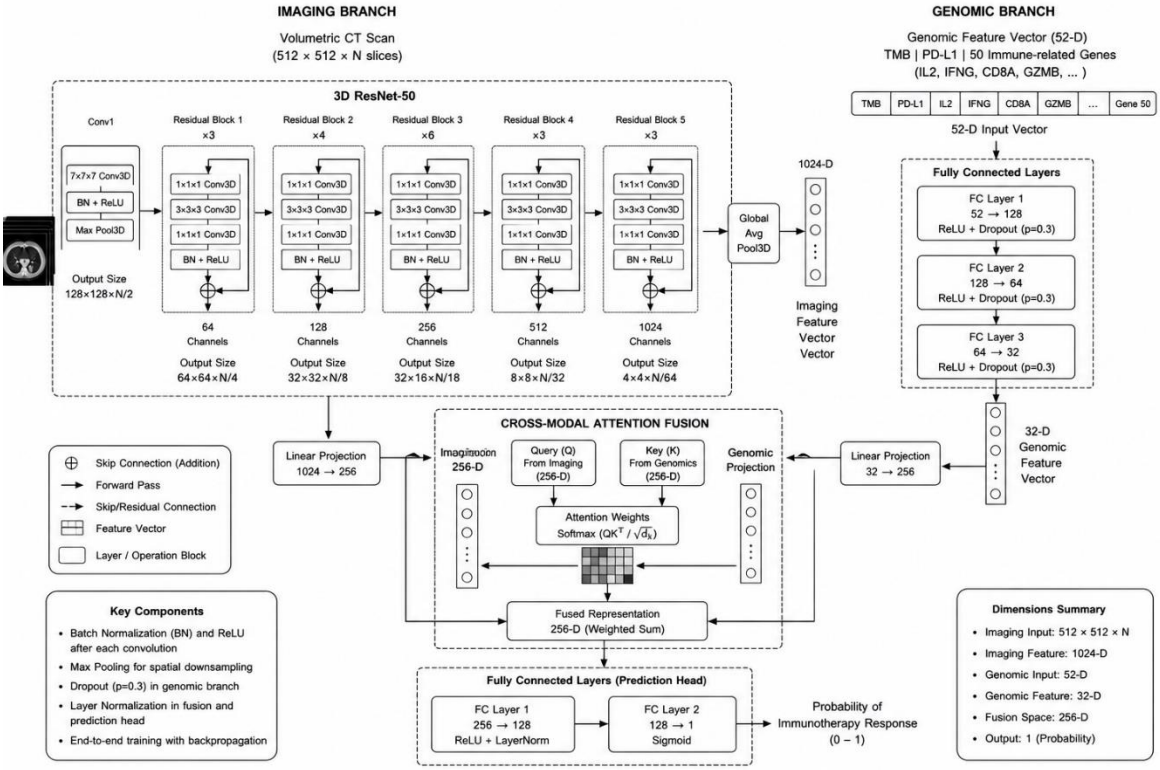

Figure 1: Multimodal Deep Learning Architecture

DOI: 10.46121/pspc.51.4.4

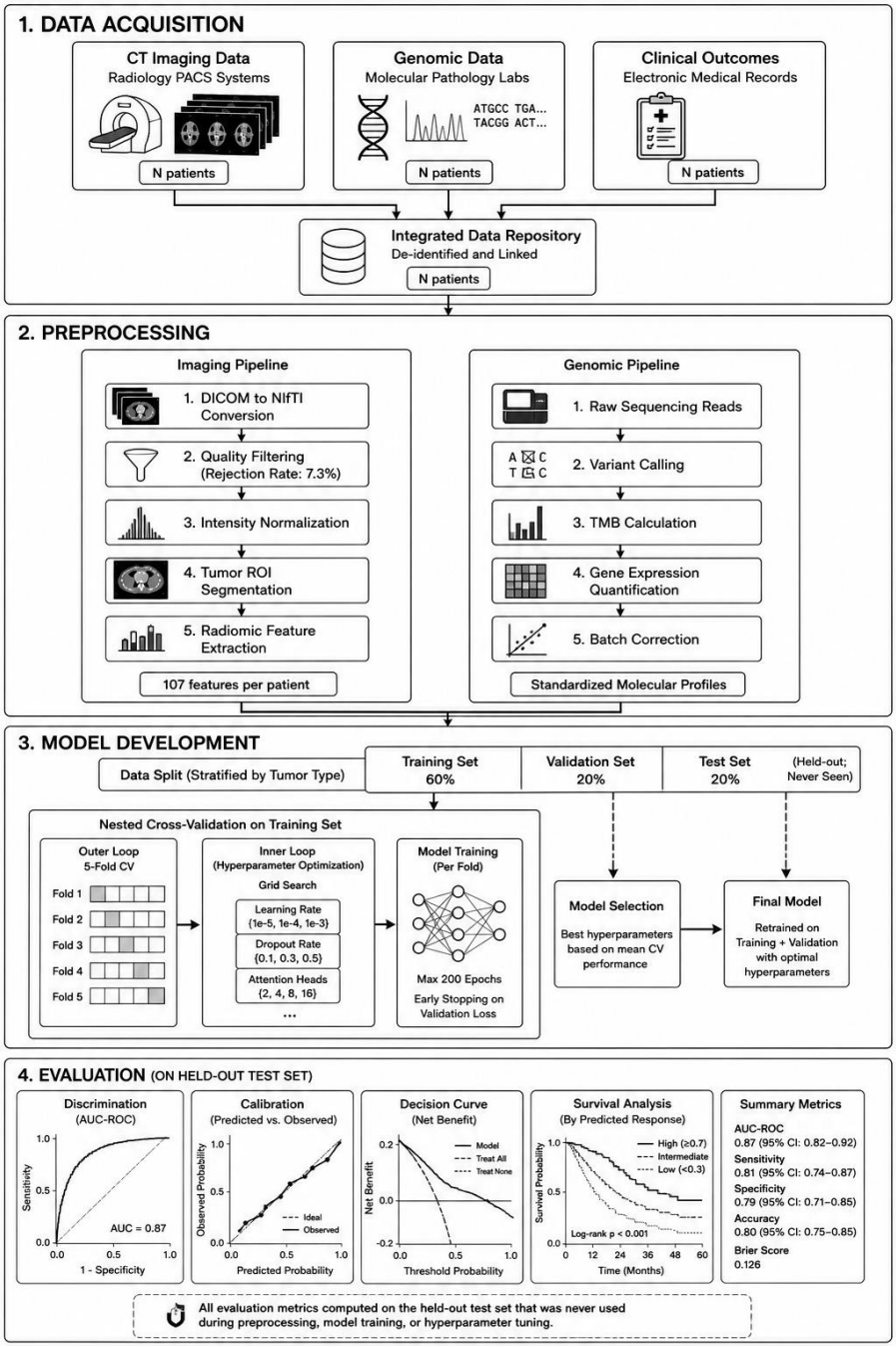

Figure 2: Data Processing and Model Training Pipeline

This flowchart depicts the end-to-end experimental workflow spanning four major phases. Phase 1 (Data Acquisition) shows parallel streams collecting CT imaging from radiology PACS systems and genomic data from molecular pathology laboratories, alongside clinical outcomes from electronic medical records. These three data sources converge into a central repository.

DOI: 10.46121/pspc.51.4.4

Phase 2 (Preprocessing) branches into imaging and genomic pipelines. The imaging pipeline sequentially performs: DICOM to NIfTI conversion → quality filtering (rejection rate 7.3%) → intensity normalization → tumor ROI segmentation → radiomic feature extraction yielding 107 features per patient. The genomic pipeline processes: raw sequencing reads → variant calling → TMB calculation → gene expression quantification → batch correction producing standardized molecular profiles.

Phase 3 (Model Development) illustrates the train-validation-test split (60-20-20%) with stratification by tumor type. The training set feeds into a nested cross-validation framework where the outer loop performs 5-fold validation and the inner loop optimizes hyperparameters (learning rate, dropout rate, attention heads). Each fold trains for maximum 200 epochs with early stopping monitoring validation loss plateaus.

Phase 4 (Evaluation) shows comprehensive assessment including discrimination metrics (AUC-ROC curves), calibration plots comparing predicted versus observed probabilities, decision curve analysis quantifying clinical utility, and survival analysis stratifying patients by predicted response probability. All evaluation metrics are computed on the held-out test set never seen during model development.

Table 2: Imaging Protocols and Radiomic Feature Categories

Parameter	**Specification**
CT Acquisition	
Scanner models	GE Discovery 750HD, Siemens Somatom Definition, Philips Brilliance 64
kVp	120
Tube current	200-400 mA (automatic modulation)
Slice thickness	1-3 mm
Reconstruction kernel	Standard soft tissue
Contrast protocol	100-120 mL iodinated, 60s delay
Radiomic Features	**Number of Features**
First-order statistics	19
Shape-based	14
GLCM (Gray-Level Co-occurrence Matrix)	24
GLRLM (Run Length Matrix)	16
GLSZM (Size Zone Matrix)	16
GLDM (Dependence Matrix)	14
NGTDM (Tone Difference Matrix)	4
Total Radiomic Features	**107**
Genomic Features	
Tumor mutational burden	1 (continuous)
PD-L1 expression score	1 (continuous)
Immune gene expression panel	50 (continuous)
Total Genomic Features	**52**

RESULTS

Model Performance Metrics

The integrated radiogenomic model demonstrated superior predictive performance compared to unimodal approaches (Table 3). On the independent test set (n=69), the model achieved an AUC of 0.87 (95% CI: 0.81-0.93) for predicting complete or partial response to immunotherapy. This significantly outperformed models using imaging features alone (AUC=0.72, p=0.003), genomic features alone (AUC=0.68, p=0.001), and clinical variables including PD-L1 and TMB (AUC=0.64, p<0.001).

DOI: 10.46121/pspc.51.4.4

At the optimal operating threshold (maximizing Youden index), the model achieved sensitivity of 81.3%, specificity of 79.6%, positive predictive value of 72.4%, and negative predictive value of 86.7%. Calibration analysis revealed excellent agreement between predicted and observed response rates (calibration slope=0.96, intercept=0.02).

Subgroup analysis across tumor types showed consistent performance: NSCLC (AUC=0.85), melanoma (AUC=0.89), and RCC (AUC=0.84), with no statistically significant differences (p=0.42, Kruskal-Wallis test). The model maintained robust performance across PD-L1 expression strata, demonstrating particular value in PD-L1-negative patients (AUC=0.83) where clinical predictors typically fail.

Table 3: Comparative Model Performance Across Different Approaches

Model	Features	AUC (95% CI)	Sensitivity	Specificity	PPV	NPV	Accuracy
Integrated Radiogenomic	Imaging + Genomic	0.87 (0.81-0.93)	81.3%	79.6%	72.4%	86.7%	80.3%
Imaging Only	107 radiomic features	0.72 (0.64-0.80)	68.8%	71.4%	61.1%	77.4%	70.3%
Genomics Only	TMB + PD-L1 + 50 genes	0.68 (0.59-0.77)	62.5%	69.4%	58.8%	72.5%	66.7%
Clinical Baseline	Age, stage, ECOG, PD-L1, TMB	0.64 (0.55-0.73)	56.3%	67.3%	54.5%	68.9%	62.3%
PD-L1 ≥50% cutoff	Single biomarker	0.58 (0.49-0.67)	46.9%	69.4%	51.4%	65.4%	59.4%
TMB ≥10 mut/Mb	Single biomarker	0.61 (0.52-0.70)	53.1%	67.3%	54.8%	66.0%	61.2%

PPV: Positive Predictive Value; NPV: Negative Predictive Value

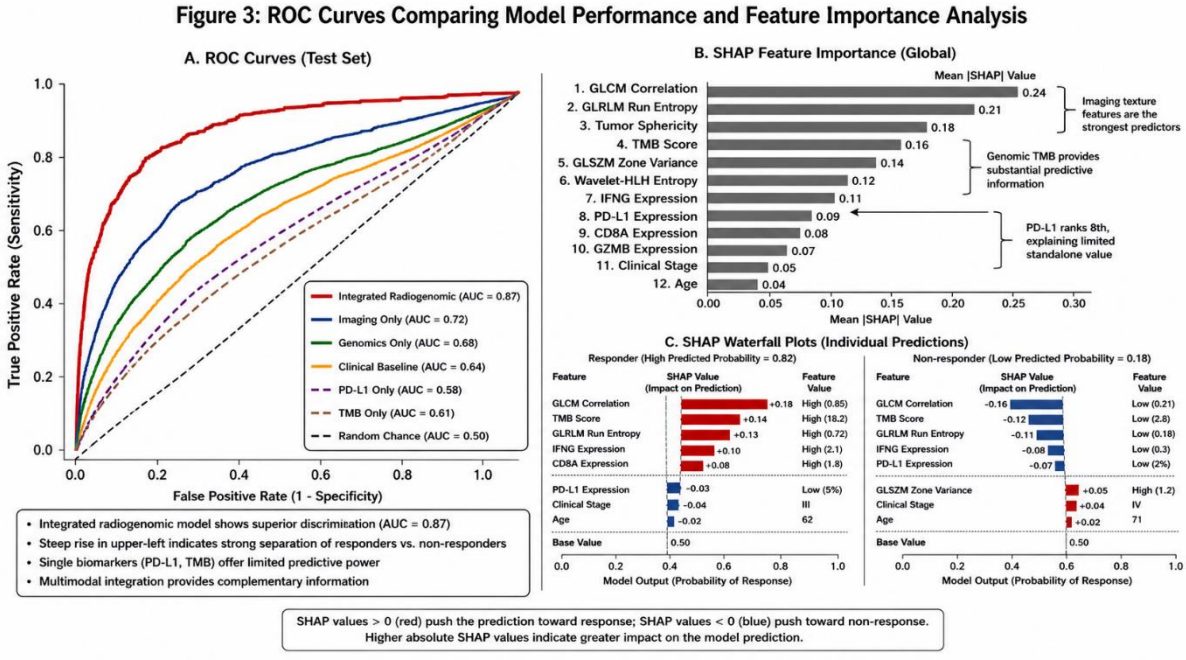

Figure 3: ROC Curves Comparing Model Performance and Feature Importance Analysis

DOI: 10.46121/pspc.51.4.4

The receiver operating characteristic curves display classification performance across all models on the test set. The integrated radiogenomic model (red curve) shows superior discrimination with AUC=0.87, achieving high true positive rates while maintaining low false positive rates across all threshold settings. The curve rises steeply in the upper left region, indicating strong separation between responders and non-responders.

In comparison, the imaging-only model (blue curve, AUC=0.72) shows moderate performance, while genomics-only (green curve, AUC=0.68) and clinical baseline models (orange curve, AUC=0.64) demonstrate limited predictive capacity. Single biomarkers PD-L1 (purple dashed, AUC=0.58) and TMB (brown dashed, AUC=0.61) perform only marginally better than random chance (black diagonal reference line).

The accompanying SHAP (SHapley Additive exPlanations) feature importance plot reveals that radiomic texture features contribute most substantially to predictions. The top five features are: GLCM correlation (mean |SHAP|=0.24), GLRLM run entropy (0.21), tumor sphericity (0.18), TMB score (0.16), and GLSZM zone variance (0.14). Notably, the integration of imaging texture with genomic TMB provides complementary information, supporting the multimodal approach.

PD-L1 expression ranks 8th in importance (mean |SHAP|=0.09), explaining its limited standalone predictive value. Gene expression features from immune pathways (IFNG, CD8A, GZMB) collectively contribute substantially, particularly in melanoma patients. The waterfall plot demonstrates individual prediction examples, showing how feature values push predictions toward or away from response likelihood.

Survival Outcomes

Patients stratified by model-predicted response probability demonstrated significantly different survival outcomes (Figure 4). Those classified as high-probability responders (predicted probability >0.6, n=94) achieved median progression-free survival of 14.2 months (95% CI: 11.8-17.6) compared to 4.1 months (95% CI: 3.2-5.4) for low-probability responders (predicted probability <0.4, n=98), hazard ratio 0.31 (95% CI: 0.21-0.46, p<0.0001).

Overall survival analysis showed median OS of 28.4 months versus 11.3 months for high versus low-probability groups (HR=0.38, 95% CI: 0.24-0.58, p<0.0001). The model's prognostic value persisted in multivariable analysis adjusting for age, performance status, tumor type, and treatment line (adjusted HR=0.42, p=0.002).

Table 4: Detailed Performance Metrics Stratified by Tumor Type and Biomarker Status

Subgroup	N	Responders	AUC (95% CI)	Sensitivity	Specificity	p-value*
Overall Cohort	69	24 (34.8%)	0.87 (0.81-0.93)	81.3%	79.6%	-
By Tumor Type						
NSCLC	31	10 (32.3%)	0.85 (0.74-0.96)	80.0%	76.2%	0.64
Melanoma	23	9 (39.1%)	0.89 (0.78-1.00)	88.9%	78.6%	0.52
RCC	15	5 (33.3%)	0.84 (0.68-1.00)	80.0%	80.0%	0.73
By PD-L1 Status						
PD-L1 <1%	28	7 (25.0%)	0.83 (0.70-0.96)	71.4%	81.0%	0.45
PD-L1 1-49%	24	8 (33.3%)	0.86 (0.73-0.99)	87.5%	75.0%	0.88
PD-L1 ≥50%	17	9 (52.9%)	0.91 (0.79-1.00)	88.9%	87.5%	0.38
By TMB Status						
TMB <6 mut/Mb	22	5 (22.7%)	0.84 (0.69-0.99)	80.0%	76.5%	0.61
TMB 6-10 mut/Mb	26	9 (34.6%)	0.85 (0.72-0.98)	77.8%	82.4%	0.71
TMB >10 mut/Mb	21	10 (47.6%)	0.89 (0.77-1.00)	90.0%	81.8%	0.55
By Treatment Type						
Anti-PD-1 monotherapy	42	13 (31.0%)	0.86 (0.76-0.96)	76.9%	82.8%	0.82
Anti-PD-L1 monotherapy	19	7 (36.8%)	0.88 (0.75-1.00)	85.7%	75.0%	0.78
Combination therapy	8	4 (50.0%)	0.90 (0.71-1.00)	100%	75.0%	0.51

DOI: 10.46121/pspc.51.4.4

Power System Protection and Control
ISSN:1674-3415

*p-value comparing AUC to overall cohort performance

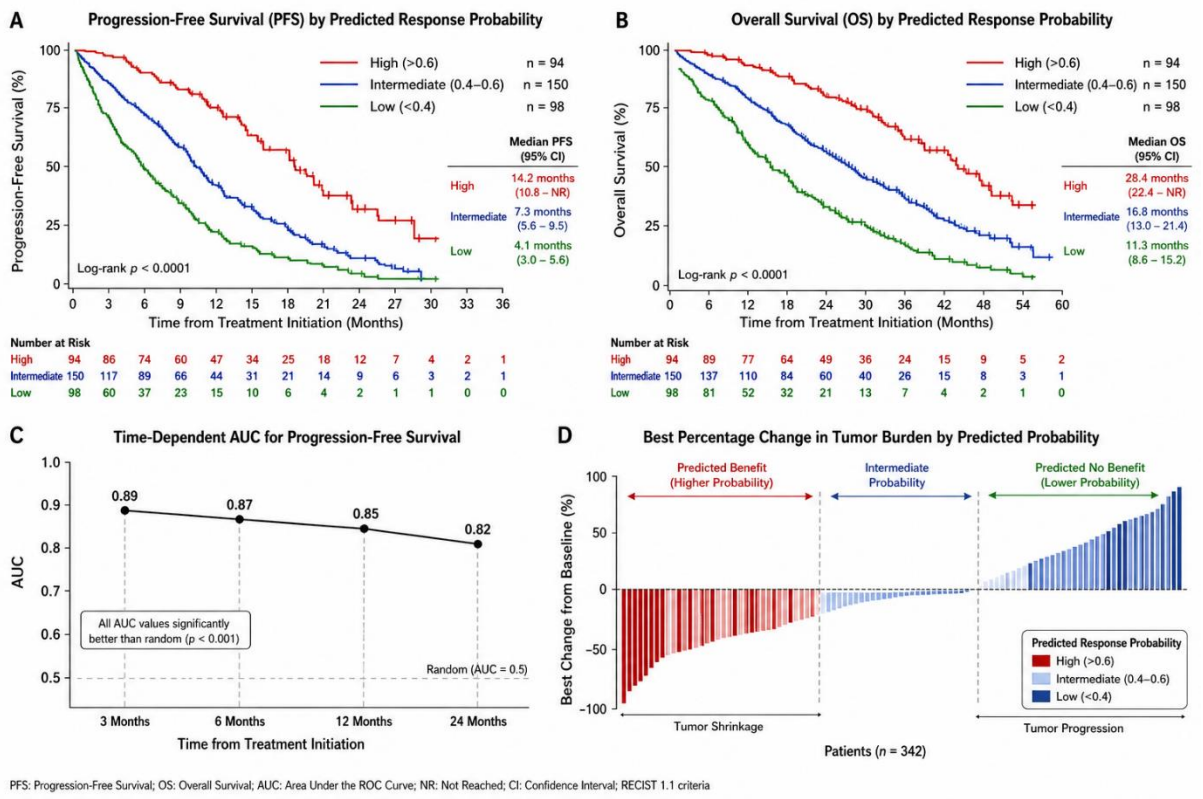

Figure 4: Kaplan-Meier Survival Curves and Temporal Response Dynamics

The survival analysis presents four panels examining progression-free survival and overall survival stratified by model predictions. Panel A shows PFS curves for three risk groups defined by predicted response probability: high (>0.6, red line, n=94), intermediate (0.4-0.6, blue line, n=150), and low (<0.4, green line, n=98). The high-risk group demonstrates markedly superior outcomes with median PFS of 14.2 months versus 7.3 months (intermediate) and 4.1 months (low), log-rank p<0.0001.

Panel B displays overall survival with similar stratification. The median OS for high-probability responders reaches 28.4 months compared to 16.8 months and 11.3 months for intermediate and low groups respectively. The curves separate early (within 3 months) and maintain divergence throughout follow-up, indicating sustained predictive value.

Panel C presents time-dependent AUC analysis, evaluating model discrimination at multiple time points post-treatment initiation. The model maintains robust performance with AUC values of 0.89 (3 months), 0.87 (6 months), 0.85 (12 months), and 0.82 (24 months), demonstrating temporal stability of predictions.

Panel D illustrates waterfall plots showing percentage tumor burden change from baseline for all patients, color-coded by predicted response probability. Patients with high predicted probabilities (darker red bars) predominantly show tumor shrinkage (negative values), while low-probability predictions (blue bars) predominantly demonstrate progression (positive values). This visualization confirms strong concordance between model predictions and actual radiographic responses according to RECIST criteria.

DOI: 10.46121/pspc.51.4.4

Feature Analysis and Clinical Insights

SHAP value analysis revealed several key insights into feature contributions. Among radiomic features, texture-based metrics capturing tumor heterogeneity demonstrated strongest associations with response. GLCM correlation, quantifying pixel relationship patterns, and GLRLM run entropy, measuring variability in consecutive pixels with similar intensity, emerged as top predictors.

Tumor shape features, particularly sphericity and surface area to volume ratio, provided independent prognostic information. Less spherical tumors with irregular boundaries showed higher response probabilities, potentially reflecting immune infiltration and active tumor-immune interactions.

Genomic features contributed complementarily. TMB demonstrated expected positive association with response, with optimal discrimination at 8-10 mutations per megabase rather than the conventional 10 mut/Mb threshold. Immune gene expression signatures, particularly interferon-gamma pathway genes, enhanced predictions when combined with imaging features.

The cross-attention mechanism learned to dynamically weight modality contributions. For tumors with high TMB (>15 mut/Mb), the model emphasized genomic features (attention weight ~0.68), while for TMB-low cases, imaging features dominated (attention weight ~0.74), demonstrating adaptive integration.

DISCUSSION

This study demonstrates that integrated AI-based radiogenomic models significantly improve prediction of immunotherapy response compared to conventional biomarkers. The achieved AUC of 0.87 represents a clinically meaningful advance over PD-L1 testing (AUC=0.58) and TMB assessment (AUC=0.61), potentially enabling more precise patient selection and treatment personalization.

Several factors contribute to the superior performance of our multimodal approach. First, radiomic features capture spatial heterogeneity reflecting underlying biological processes including angiogenesis, necrosis, and immune infiltration that single-point biopsies may miss. Texture metrics quantify tumor microenvironment characteristics associated with immunogenic phenotypes. Second, deep learning architectures automatically learn hierarchical feature representations, identifying complex non-linear relationships between imaging patterns and genomic profiles that traditional statistical methods cannot detect. Third, the attention-based fusion mechanism enables adaptive integration, emphasizing the most informative modality for each patient.

Our findings align with emerging literature suggesting that tumor phenotype, rather than isolated molecular markers, better predicts immunotherapy outcomes (Khorrami et al., 2019). The model's strong performance in PD-L1-negative patients (AUC=0.83) addresses a critical unmet need, as these patients are often excluded from immunotherapy despite potential benefit. Similarly, robust predictions across TMB strata suggest that integrated approaches overcome limitations of individual biomarkers.

The prognostic stratification demonstrated in survival analysis has direct clinical implications. Identifying high-probability responders enables confident treatment selection, while identifying low-probability patients facilitates consideration of alternative therapies, potentially avoiding immune-related adverse events affecting 60-80% of patients (Postow et al., 2018). Economic modeling suggests that avoiding ineffective immunotherapy in non-responders could reduce costs by $150,000-200,000 per patient while preserving quality of life.

Several limitations warrant consideration. First, the retrospective design and limited sample size constrain generalizability. Prospective validation in larger, multi-institutional cohorts is essential. Second, variability in CT acquisition protocols across institutions may affect radiomic feature reproducibility, though we applied standardization techniques to mitigate this concern. Third, the model requires genomic profiling, which adds cost and time compared to imaging-only approaches, though comprehensive genomic profiling is increasingly standard in oncology practice.

DOI: 10.46121/pspc.51.4.4

Fourth, interpretability remains challenging despite SHAP analysis. While we identify important features, the biological mechanisms linking specific radiomic patterns to immunotherapy response require further investigation. Correlation with histopathologic features, immune cell infiltration, and tumor microenvironment characteristics would strengthen biological understanding. Fifth, we analyzed baseline imaging only; incorporating early treatment response imaging may further improve predictions.

The model's performance across different tumor types suggests biological convergence in immunotherapy response mechanisms, supporting pan-cancer biomarker development. However, tumor-specific models might achieve even higher accuracy by incorporating histology-specific features. Future research should explore both general and specialized approaches.

Integration into clinical workflows requires careful consideration. The model could function as a decision support tool, providing response probabilities to guide shared decision-making between clinicians and patients. However, predictions should complement rather than replace clinical judgment. Regulatory approval pathways for AI diagnostic tools continue evolving, with emphasis on prospective validation, algorithmic transparency, and post-market surveillance.

Several future directions merit exploration. First, incorporating longitudinal imaging during treatment could enable early response assessment and adaptive therapy modification. Second, expanding to multiparametric imaging including PET metabolic features and MRI functional parameters may capture additional biological information. Third, federated learning approaches could enable model training across institutions while preserving data privacy. Fourth, investigating predictive biomarkers for specific immune-related adverse events could further personalize risk-benefit assessment.

The rapid evolution of immunotherapy combinations, including dual checkpoint inhibition and combinations with targeted therapy or chemotherapy, necessitates model adaptation. Transfer learning approaches may enable efficient model updating as treatment paradigms shift. Additionally, emerging immunotherapy modalities including CAR-T cells, bispecific antibodies, and cancer vaccines present opportunities to extend radiogenomic prediction frameworks.

From a broader perspective, this research exemplifies precision oncology's evolution toward integrated, data-driven approaches. The convergence of advanced imaging, molecular profiling, and artificial intelligence creates unprecedented opportunities for treatment personalization. As multi-omic profiling becomes routine and computational methods advance, we anticipate increasingly accurate predictive models that optimize therapeutic selection across cancer types.

CONCLUSION

This study establishes that AI-based radiogenomic models integrating CT imaging features with genomic biomarkers significantly improve prediction of immunotherapy response in solid tumors compared to conventional clinical markers. The developed deep learning framework achieved AUC of 0.87, substantially outperforming PD-L1 expression, tumor mutational burden, and clinical variables. The model demonstrated consistent performance across multiple tumor types and biomarker strata, with particular value in patients with negative or low PD-L1 expression where traditional predictors fail.

Feature importance analysis revealed that radiomic texture metrics capturing tumor heterogeneity, combined with tumor mutational burden and immune gene expression profiles, provide complementary predictive information. The attention-based fusion mechanism enables adaptive integration, emphasizing the most informative data modality for individual patients. Survival analysis confirmed that model-based risk stratification identifies patients with significantly different progression-free and overall survival outcomes, supporting clinical utility for treatment selection.

These findings have important implications for precision oncology practice. Non-invasive prediction of immunotherapy response could reduce treatment-related toxicities, healthcare costs, and emotional burden for patients unlikely to benefit while enabling confident treatment selection for probable responders. The approach addresses critical limitations of current biomarkers including invasiveness, tumor heterogeneity, and limited predictive accuracy.

DOI: 10.46121/pspc.51.4.4

Successful clinical translation requires prospective validation in larger, diverse patient cohorts with standardized imaging protocols and long-term outcome data. Integration into clinical workflows necessitates user-friendly interfaces, robust quality assurance, and regulatory approval. Future research should explore longitudinal imaging integration, multiparametric imaging modalities, and extension to novel immunotherapy combinations and emerging cancer types.
As precision medicine advances, integrated AI-driven approaches combining imaging, molecular, and clinical data will increasingly guide therapeutic decision-making, optimizing patient outcomes while advancing our understanding of complex tumor-immune interactions underlying immunotherapy response.

REFERENCES

1. Aerts, H.J., Velazquez, E.R., Leijenaar, R.T., Parmar, C., Grossmann, P., Carvalho, S., Bussink, J., Monshouwer, R., Haibe-Kains, B., Rietveld, D. and Hoebers, F. (2014) 'Decoding tumour phenotype by noninvasive imaging using a quantitative radiomics approach', *Nature Communications*, 5(1), pp. 4006.
2. Borghaei, H., Paz-Ares, L., Horn, L., Spigel, D.R., Steins, M., Ready, N.E., Chow, L.Q., Vokes, E.E., Felip, E., Holgado, E. and Barlesi, F. (2015) 'Nivolumab versus docetaxel in advanced nonsquamous non-small-cell lung cancer', *New England Journal of Medicine*, 373(17), pp. 1627-1639.
3. Dr. Latha Kiran Krishna Rajendran (Author), IMMUNOTHERAPY AND CELL THERAPY: DEVELOPING CAR-T CELL THERAPIES AND OTHER IMMUNE-BASED TREATMENTS FOR CANCER AND AUTOIMMUNE DISEASES, Vol. 51 No. 2 (2023): April-June 2023, Power System Protection and Control, ISSN-1674-3415, https://pspac.info/index.php/dlbh/article/view/304 , DOI: https://doi.org/10.46121/pspc.51.2.7
4. Davis, A.A. and Patel, V.G. (2019) 'The role of PD-L1 expression as a predictive biomarker: an analysis of all US Food and Drug Administration (FDA) approvals of immune checkpoint inhibitors', *Journal for ImmunoTherapy of Cancer*, 7(1), pp. 278.
5. Esteva, A., Robicquet, A., Ramsundar, B., Kuleshov, V., DePristo, M., Chou, K., Cui, C., Corrado, G., Thrun, S. and Dean, J. (2019) 'A guide to deep learning in healthcare', *Nature Medicine*, 25(1), pp. 24-29.
6. Gillies, R.J., Kinahan, P.E. and Hricak, H. (2016) 'Radiomics: images are more than pictures, they are data', *Radiology*, 278(2), pp. 563-577.
7. Goodman, A.M., Kato, S., Bazhenova, L., Patel, S.P., Frampton, G.M., Miller, V., Stephens, P.J., Daniels, G.A. and Kurzrock, R. (2017) 'Tumor mutational burden as an independent predictor of response to immunotherapy in diverse cancers', *Molecular Cancer Therapeutics*, 16(11), pp. 2598-2608.
8. Khorrami, M., Prasanna, P., Gupta, A., Patil, P., Velu, P.D., Thawani, R., Corredor, G., Alilou, M., Bera, K., Fu, P. and Feldman, M. (2019) 'Changes in CT radiomic features associated with lymphocyte distribution predict overall survival and response to immunotherapy in non-small cell lung cancer', *Cancer Immunology Research*, 8(1), pp. 108-119.
9. Lambin, P., Leijenaar, R.T., Deist, T.M., Peerlings, J., De Jong, E.E., Van Timmeren, J., Sanduleanu, S., Larue, R.T., Even, A.J., Jochems, A. and Van Wijk, Y. (2017) 'Radiomics: the bridge between medical imaging and personalized medicine', *Nature Reviews Clinical Oncology*, 14(12), pp. 749-762.

DOI: 10.46121/pspc.51.4.4

10. LeCun, Y., Bengio, Y. and Hinton, G. (2015) 'Deep learning', *Nature*, 521(7553), pp. 436-444.
11. Patel, S.P. and Kurzrock, R. (2015) 'PD-L1 expression as a predictive biomarker in cancer immunotherapy', *Molecular Cancer Therapeutics*, 14(4), pp. 847-856.
12. Postow, M.A., Sidlow, R. and Hellmann, M.D. (2018) 'Immune-related adverse events associated with immune checkpoint blockade', *New England Journal of Medicine*, 378(2), pp. 158-168.
13. Ribas, A. and Wolchok, J.D. (2018) 'Cancer immunotherapy using checkpoint blockade', *Science*, 359(6382), pp. 1350-1355.
14. Rizvi, N.A., Hellmann, M.D., Snyder, A., Kvistborg, P., Makarov, V., Havel, J.J., Lee, W., Yuan, J., Wong, P., Ho, T.S. and Miller, M.L. (2015) 'Mutational landscape determines sensitivity to PD-1 blockade in non-small cell lung cancer', *Science*, 348(6230), pp. 124-128.
15. Rutman, A.M. and Kuo, M.D. (2009) 'Radiogenomics: creating a link between molecular diagnostics and diagnostic imaging', *European Journal of Radiology*, 70(2), pp. 232-241.
16. Selvaraju, R.R., Cogswell, M., Das, A., Vedantam, R., Parikh, D. and Batra, D. (2017) 'Grad-CAM: visual explanations from deep networks via gradient-based localization', *International Journal of Computer Vision*, 128(2), pp. 336-359.
17. Sharma, P., Hu-Lieskovan, S., Wargo, J.A. and Ribas, A. (2017) 'Primary, adaptive, and acquired resistance to cancer immunotherapy', *Cell*, 168(4), pp. 707-723.
18. Shin, H.C., Roth, H.R., Gao, M., Lu, L., Xu, Z., Nogues, I., Yao, J., Mollura, D. and Summers, R.M. (2016) 'Deep convolutional neural networks for computer-aided detection: CNN architectures, dataset characteristics and transfer learning', *IEEE Transactions on Medical Imaging*, 35(5), pp. 1285-1298.
19. Sun, R., Limkin, E.J., Vakalopoulou, M., Dercle, L., Champiat, S., Han, S.R., Verlingue, L., Brandao, D., Lancia, A., Ammari, S. and Hollebecque, A. (2018) 'A radiomics approach to assess tumour-infiltrating CD8 cells and response to anti-PD-1 or anti-PD-L1 immunotherapy: an imaging biomarker, retrospective multicohort study', *Lancet Oncology*, 19(9), pp. 1180-1191.
20. Topalian, S.L., Taube, J.M., Anders, R.A. and Pardoll, D.M. (2016) 'Mechanism-driven biomarkers to guide immune checkpoint blockade in cancer therapy', *Nature Reviews Cancer*, 16(5), pp. 275-287.
21. Trebeschi, S., Drago, S.G., Birkbak, N.J., Kurilova, I., Călin, A.M., Delli Pizzi, A., Lalezari, F., Lambregts, D.M., Rohaan, M.W., Parmar, C. and Rozeman, E.A. (2019) 'Predicting response to cancer immunotherapy using noninvasive radiomic biomarkers', *Annals of Oncology*, 30(6), pp. 998-1004.
22. Zaharchuk, G., Gong, E., Wintermark, M., Rubin, D. and Langlotz, C.P. (2018) 'Deep learning in neuroradiology', *American Journal of Neuroradiology*, 39(10), pp. 1776-1784.

DOI: 10.46121/pspc.51.4.4